

Modeling depletion mediated colloidal assembly on topographical patterns



Yuguang Yang, Tara D. Edwards, Michael A. Bevan^{*}

Chemical & Biomolecular Engineering, Johns Hopkins University, Baltimore, MD 21218, United States

ARTICLE INFO

Article history:

Received 1 November 2014

Accepted 1 December 2014

Available online 6 December 2014

Keywords:

Tunable depletion attraction

Patterned excluded volume

Reconfigurable colloidal assembly

Monte Carlo simulations

Non-close packed structures

ABSTRACT

This work reports a model and Monte Carlo simulations of excluded volume mediated interactions between colloids and topographically patterned substrates in the presence of thermosensitive depletants. The model is matched to experiments to yield density, free energy, and potential energy landscapes that quantitatively capture particle microstructures varying from immobilized non-close packed configurations to random fluid states. A numerical model of local excluded volume effects is developed to enable computation of local depletion attraction in the presence of arbitrary geometries. Our findings demonstrate a quantitative modeling method to interpret and predict how surface patterns mediate local depletion interactions, which enables the design of colloidal based materials and devices.

© 2014 Elsevier Inc. All rights reserved.

1. Introduction

Depletion interactions arise between colloids and surfaces from “solute particles” being depleted, or excluded, from the gap between interacting objects [1]. When this occurs, pure solvent in the excluded volume has a different chemical potential from the solution outside the excluded volume. This produces an attraction between particles and surfaces proportional to the product of osmotic pressure and the excluded volume. Although depletion potentials become more complicated based on how solute particles interact with each other and surfaces [2], the basic picture presented above qualitatively captures the mechanism of colloidal depletion attraction for diverse solutes (e.g., polymers, micelles, hydrogel particles, nanoparticles [3]). Because depletion interactions can occur in any mixture when a solute is excluded between surfaces, such interactions are expected to be ubiquitous in complex industrial formulations as well as biological systems [4].

By understanding the mechanism of depletion attraction, there is an opportunity to design such potentials by either controlling the osmotic pressure or designing the excluded volume. Examples of tuning the depletant osmotic pressure have included thermosensitive micelles [5], hydrogel particles [6,7], and polymer chains [8]. However, in each of these examples, the osmotic pressure changes because the depletant size changes, which also means the excluded volume changes (which depends on relative depletant and colloid dimensions). Beyond tuning depletant dimensions,

exclude volume has been manipulated via surface geometries in several key examples including confining surfaces [9,10], surface features [11], templates for crystallization [12,13], surface roughness [14,15], and lock-and-key colloids (i.e., local curvature) [16]. Although such studies demonstrate clever examples of tuning depletion interactions to affect colloidal assembly, accurate models have not been sufficiently developed to allow for systematic design and control of surface geometries that mediate local depletion potentials in colloidal materials and devices.

Here we report the development of a new method to compute local excluded volume and depletion interactions between particles and physically patterned surfaces. This method is used to analyze measurements of temperature dependent particle configurations on microfabricated surface topographies in the presence of thermosensitive depletants. Specifically, we analyze particles interacting with arrays of circles with sloping walls that produce additional local excluded volume (left side of Fig. 1, experiments reported elsewhere [17]). These measurements, and the new model reported here, are distinct from our prior study of patterned depletion mediated colloidal crystallization on an underlying gravitational energy landscape [7]. The present work is both scientifically and technologically novel by exploiting local excluded volume effects in conjunction with thermosensitive depletants to create non-close-packed reconfigurable structures. Such non-close-packed structures with length scales comparable to electromagnetic radiation have important applications as metamaterials and their reconfigurability can allow such systems to be used as static materials or programmable devices [18]. Ultimately, our findings demonstrate a quantitative modeling tool to

^{*} Corresponding author.

E-mail address: mabevan@jhu.edu (M.A. Bevan).

interpret and predict how local surface geometries alter local depletion interactions, which can enable new colloidal based materials and devices.

2. Theory

2.1. Net interaction potential

The net potential energy for colloidal particles interacting with each other, an underlying surface, and gravity (see Fig. 2) can be modeled as the superposition of independent potentials. For a charged colloidal particle i with radius, a , in the presence of non-adsorbing depletant particles, the net interaction potential is given by,

$$u_i(\mathbf{r}_i) = u_D^{pw}(\mathbf{r}_i) + u_E^{pw}(\mathbf{r}_i) + u_G^{pf}(z_i) + \sum_{j \neq i} [u_D^{pp}(r_{ij}) + u_E^{pp}(r_{ij})] \quad (1)$$

where $\mathbf{r}_i = (x_i, y_i, z_i)$ is position vector of particle i , z_i is the particle center-to-surface elevation relative to the underlying surface, and r_{ij} is center-to-center separation between particles i and j . Subscripts refer to: (E) electrostatic, (G) gravitational, and (D) depletion, and superscripts refer to: (pp) particle–particle, (pw) particle–wall, and (pf) particle–field. The range of electrostatic repulsion in this work is sufficient so that van der Waals interactions can be neglected.

2.2. Gravitational potential

The gravitational potential energy of each particle depends on its elevation above the reference surface multiplied by its buoyant weight, G , given by,

$$u_G^{pf}(z) = Gz = (4/3)\pi a^3(\rho_p - \rho_f)gz \quad (2)$$

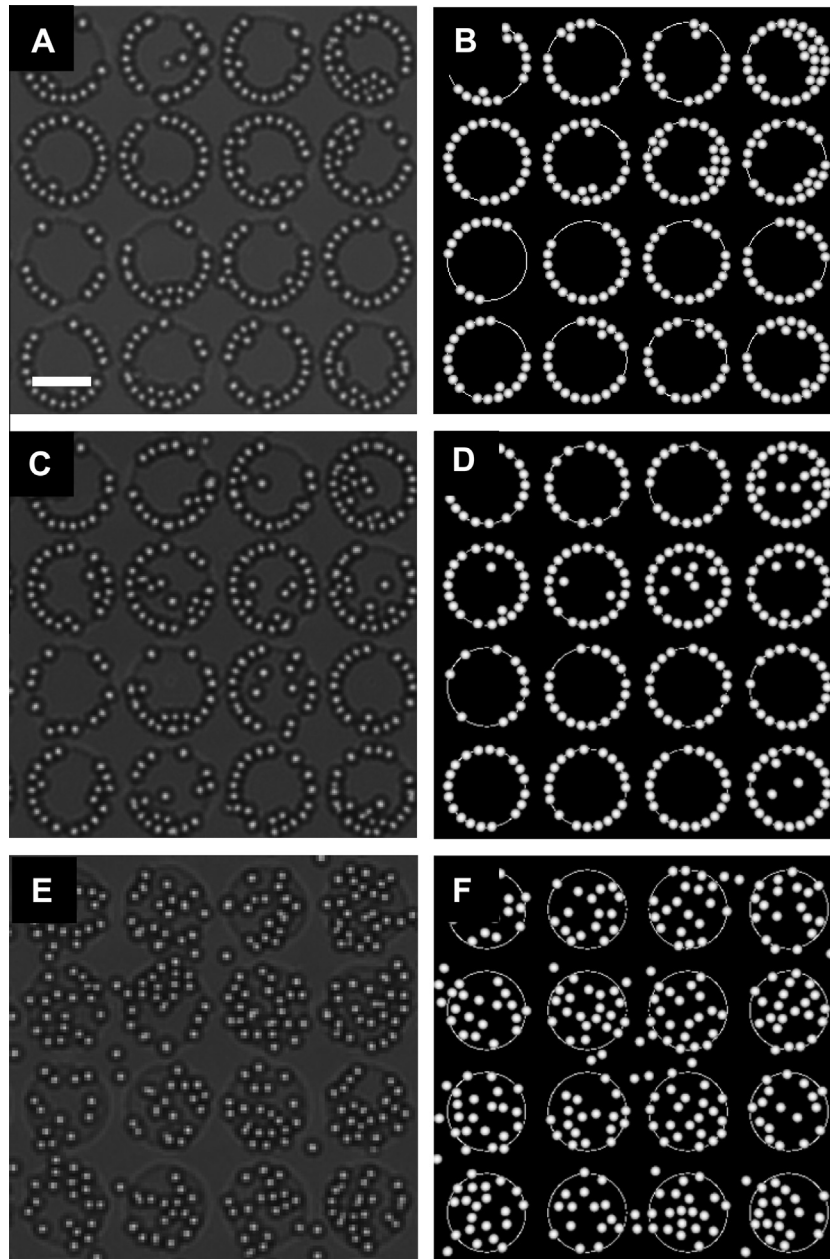


Fig. 1. Experimental images (A, C, E) and simulation renderings (B, D, F) of charged $\sim 2 \mu\text{m}$ SiO_2 colloids at 0.18 area fraction experiencing depletion attraction with each other and a topographically patterned (well depth $H = 285 \text{ nm}$) glass microscope slide surface. The depletion potential is tuned by the depletant size, $2L$, at 25°C , $2L = 113 \text{ nm}$ (A, B), 35°C , $2L = 107 \text{ nm}$ (C, D), 37°C , $2L = 53 \text{ nm}$ (E, F).

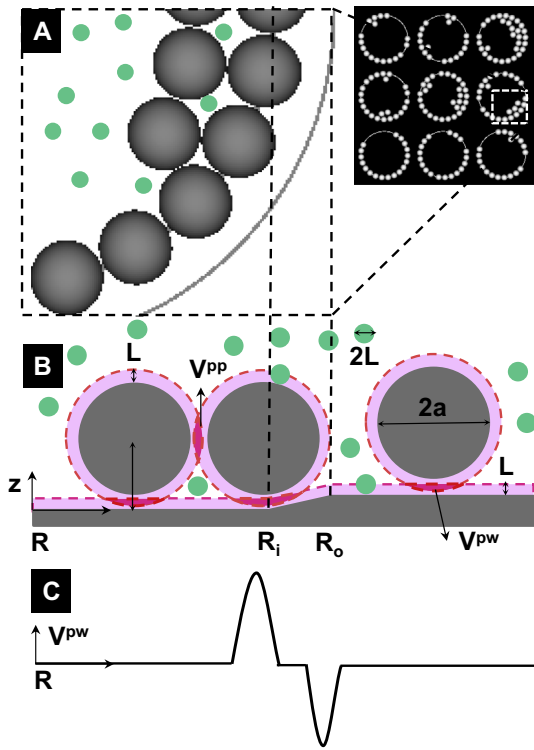


Fig. 2. Schematics of substrate geometry. (A) Snapshot (top views) of simulation rendering and magnified view of particles at pattern edge. (B) Cross sectional view of particles at pattern edge. Green and gray spheres are depletants and colloids. Red band (light) surrounding the gray sphere and the gray substrate is excluded volume (approximated via hard sphere repulsion). (C) Qualitative profiles of particle–wall excluded volume vs. radial coordinate from pattern feature center to edge and beyond (for colloidal sphere at constant elevation above substrate). (For interpretation of the references to color in this figure legend, the reader is referred to the web version of this article.)

where g is acceleration due to gravity, and ρ_p and ρ_f are the particle and fluid densities.

2.3. Electrostatic interaction potentials

The colloidal particles are electrostatically stabilized against aggregation and deposition due to van der Waals attraction. The interaction between electrostatic double layers on adjacent particle and planar wall surfaces are given by [19],

$$u_E^{pp}(r) = B \exp[-\kappa(r - 2a)], u_E^{pw}(z) = 2B \exp[-\kappa(z - a)] \quad (3)$$

$$B = 32\pi\epsilon a \left(\frac{kT}{e}\right)^2 \tanh\left(\frac{e\psi_1}{4kT}\right) \tanh\left(\frac{e\psi_2}{4kT}\right), \kappa = (2e^2 N_A C / \epsilon kT)^{1/2}$$

where κ is the inverse Debye length, ϵ is the solvent dielectric constant, k is Boltzmann's constant, T is absolute temperature, C is the 1:1 monovalent electrolyte molarity, N_A is Avogadro's number, e is the elemental charge, and ψ_1 and ψ_2 are the surface potentials.

2.4. AO depletion potentials

The depletion attraction between particles and underlying substrate surface can be given by a modified form of the usual AO depletion potential as [1],

$$u_D^{pp}(r) = -\Pi V_{EX}^{pp}(r) \quad (4)$$

$$u_D^{pw}(\mathbf{r}) = -\Pi V_{EX}^{pw}(\mathbf{r}) \quad (5)$$

where Π is the depletant osmotic pressure, and $V_{EX}^{pp}(r)$ and $V_{EX}^{pw}(\mathbf{r})$ are the excluded volume (see Fig. 1(b)) for particle–particle and particle–planar wall geometries given as [20–22],

$$V_{EX}^{pp}(r) = \pi \left[\left(\frac{4}{3} \right) (a + L)^3 \left(1 - \left(\frac{3}{4} \right) r (a + L)^{-1} + \left(\frac{1}{16} \right) r^3 (a + L)^{-3} \right) \right] \quad (6)$$

$$V_{EX}^{pw}(z) = \pi \left[\left(\frac{4}{3} \right) L^3 + 4L^2 a - 4La(z - a) + a(z - a)^2 - L(z - a)^2 + \left(\frac{1}{3} \right) (z - a)^3 \right] \quad (7)$$

where L is the depletant radius. For particles in the vicinity of a topographical pattern feature, the form of Eq. (5) remains the same in that the magnitude is determined by the depletant osmotic pressure, but the excluded volume term is computed numerically as described in the methods section of this paper. The numerical method is validated by producing the correct excluded volume terms given for particle–particle and particle–wall geometries in Eqs. (6) and (7).

2.5. Quasi-two dimensional models

In this paper, we perform quasi-2D measurements, simulations, and analyses of particles on patterned surfaces. The particles are assigned to a most probable elevation, z_M , above the substrate, which is the location of the net potential energy profile minimum normal to the substrate where the sum of the forces on the particle equal zero. This value can be determined as the value of z where the gradient of the net potential energy (z -dependent potentials in Eq. (1)) equals zero as given by,

$$\frac{\partial}{\partial z} \left[u_G^{pf}(z) + u_D^{pw}(z) + u_E^{pw}(z) \right] = 0 \quad (8)$$

This approach allows the position dependent elevation of each particle, $z(x_i, y_i)$, to be given as the sum of the local physical topography and the most probable height above the surface as,

$$z_i(x_i, y_i) = z_M + z(x_i, y_i) \quad (9)$$

which gives the net quasi-two dimensional potential energy (including a quasi-2D gravitational potential energy landscape [7,23]) for each particle as,

$$u_i(\mathbf{r}_i) = Gz_M(\mathbf{r}_i) + u_D^{pw}(\mathbf{r}_i) + \sum_{j \neq i} \left[u_E^{pp}(\mathbf{r}_{ij}) + u_D^{pp}(\mathbf{r}_{ij}) \right] \quad (10)$$

The goal of this work is to understand how particles sample the 2D energy landscape in the presence of gravity, depletion forces, and multi-particle packing effects. It has been shown that single particles (sufficiently dilute to only interact with surface but not each other) will sample the landscape in Eq. (10) via a Boltzmann relation (and its algebraic inverse) given by,

$$\rho(\mathbf{r}) / \rho_{\text{ref}} = \exp[-(u(\mathbf{r}) - u_{\text{ref}}) / kT] \quad (11)$$

$$[u(\mathbf{r}) - u_{\text{ref}}] / kT = -\ln[\rho(\mathbf{r}) / \rho_{\text{ref}}]$$

where $u(\mathbf{r})$ is the potential energy landscape in Eq. (10), and ρ_{ref} and u_{ref} are the reference density and potential at a given state and location in the system (e.g., single particle at the center of a pattern feature without any depletion attraction). For example, in the absence of particle–particle interactions or particle–wall depletion attraction, the potential energy landscape depends only on gravity and the height as,

$$u(x, y) - u_{\text{ref}} = G[z(x, y) - z_{\text{ref}}] \quad (12)$$

where z_{ref} is a reference height (e.g., lowest or highest elevation on a surface). As particles begin to interact with each other and the underlying surface at finite concentration, the distribution of particles is related to the free energy landscape, $w(\mathbf{r})$, (and its algebraic inverse) given by,

$$\begin{aligned} \rho(\mathbf{r})/\rho_{\text{ref}} &= \exp[-(w(\mathbf{r}) - w_{\text{ref}})/kT] \\ [w(\mathbf{r}) - w_{\text{ref}}]/kT &= -\ln[\rho(\mathbf{r})/\rho_{\text{ref}}] \end{aligned} \quad (13)$$

where ρ_{ref} and w_{ref} are again a reference density and potential at a given location (spatial position) and state (i.e., global thermodynamic variables).

3. Methods

3.1. Excluded volume calculation

Considering the large ratio of the well diameter to the colloid diameter, we approximate the sloping well edge in Fig. 2 as a flat plane ($R_i R_o$ section). The calculation of excluded volume is the intersection of colloidal particle excluded volume with the excluded volume from the three planes ($<R_i$, $R_i R_o$, $>R_o$ sections). The excluded volume of sphere and substrate are discretized with a resolution of $0.025a$ for each dimension (x , y , z), and then the volume elements inside the shaded region are added to obtain the overlap volume for the particle at each position (x , y , z). The accuracy of this method was validated by reproducing the particle–particle (Eq. (6)) and particle–wall (Eq. (7)) excluded volumes to $<1\%$ error.

3.2. Monte Carlo simulations

Quasi-2D experiments are modeled in 2D Monte Carlo (MC) simulations where colloids samples landscapes determine by gravity and substrate topography mediated depletion potentials. In 2D MC simulations, moves in x , y directions are accepted or rejected using the energy function in Eq. (10). In this implementation, real-time calculation of the excluded volume for every particle position would be computationally prohibitive. However, exploiting the natural system symmetry and periodicity (see Fig. 1), the particle position $[x, y, z(x, y)]$ is converted to $[R, z(R)]$, where R is the radial distance to the nearest well center. The excluded volume is then pre-calculated in a look-up table for use in the simulation. The MC simulations are performed at three different temperatures with all parameters listed in Table 1. Initial configurations for simulations were obtained from experimental images. Each MC simulation was performed for 2.5×10^6 steps with particle positions stored every 250 steps after an initial 10^6 step equilibration.

4. Results and discussion

4.1. 2D density landscapes

In experiments reported elsewhere [17] and shown in Fig. 1, temperature sensitive poly-N-isopropylacrylamide (PNIPAM) hydrogel particles were used as thermosensitive depletants to mediate depletion attraction between $\sim 2 \mu\text{m}$ SiO_2 colloids and physically patterned surfaces. The temperature dependent PNIPAM depletant size produces tunable excluded volumes and depletant osmotic pressures to tune the net depletion potential. These tunable potentials provided the capability to control reconfiguration of colloidal particles between isotropic and non-close packed structures on a variety of topographical features. Here we report potentials and simulation methods that quantitatively capture these experimental observations and provide the capability to design new systems that exploit these tunable interactions and local excluded volume effects.

We first compare time-averaged equilibrium configurations from microscopy experiments and MC simulations for the three temperatures reported in Fig. 1. The 2D density profiles, $\rho(x, y)$, are normalized by the maximum density and are reported in Fig 3. The

Table 1

Parameters for MC simulations to match with experiments.

| Variable | Theory/simulation |
|--------------------------------------|---------------------|
| a/nm^a | 1100 |
| κ^{-1}/nm^b | 9.54 |
| ψ/mV^c | −50 |
| $T/^\circ\text{C}^d$ | 25, 35.0, 37.0 |
| $2R/\mu\text{m}^e$ | 17 |
| $D/\mu\text{m}^f$ | 21 |
| H/nm^g | 285 |
| $2L/\text{nm}^h$ | 113, 107, 53 |
| $\Pi/kT (10^{-7} \text{ nm}^{-3})^i$ | 26.0, 18.0, 5.4 |
| $\rho (10^{-7} \text{ nm}^{-3})^j$ | 4.8, 4.6, 4.7 |
| ϕ_D^k | 0.36, 0.30, 0.37 |
| z_m/nm^l | 61, 66, 100 |
| $\phi_{A,C}^m$ | 0.178, 0.178, 0.175 |
| N^n | 332, 332, 324 |

^a Colloidal particle size.

^b Debye screening length.

^c Particle and wall electrostatic potential [26,27].

^d Temperature.

^e Patterned circle diameter.

^f Center-to-center pattern spacing.

^g Patterned depth.

^h Depletant size.

ⁱ Depletant osmotic pressure.

^j Depletant number density.

^k Depletant volume fraction.

^l Most probable height.

^m Colloidal particle area fraction.

ⁿ Colloidal particle number.

experimental $\rho(x, y)$ were constructed from 50,156 images in 30 min videos (as reported in our separate experimental paper [17]). Most parameters used in the MC simulations were measured independently and reported in Table 1. To match experiment and MC simulations for each temperature, the particle–pattern excluded volume was computed using the numerical technique described in the methods section, which left the PNIPAM osmotic pressure as the sole adjustable parameter. The initial guess for the PNIPAM osmotic pressure was based on the Carnahan–Starling equation of state (CS–EOS) and DLS measured PNIPAM sizes [6,7]. Table 1 lists the temperature independent depletant number density and temperature dependent depletant volume fractions obtained from the fitted osmotic pressure values and the CS–EOS, which are reasonable based on the PNIPAM solution preparation.

Fig. 3 shows excellent agreement is observed between experiments and simulations at each temperature (within the statistical and spatial resolution of the experiments). Parts A, B in Figs. 1 and 3 show that for the largest depletant size ($2L = 113 \text{ nm}$) at the lowest temperature ($T = 25^\circ\text{C}$), particles preferentially stick to pattern feature edge where the excluded volume is the greatest. Depending on the number of particles in the well, a second ring of particle forms via lateral particle–particle depletion attraction. As temperature increases ($T = 35^\circ\text{C}$) and depletant size slightly decreases ($2L = 107 \text{ nm}$) in parts C, D in Figs. 1 and 3, particles near the pattern feature display an almost imperceptible increase in thermal motion and the second ring of particles now sample the pattern feature interior. Both effects show that reduced depletant size weakens the depletion attraction from a smaller excluded volume and a smaller depletant osmotic pressure (which scales as depletant volume, e.g., second virial coefficient, volume fraction in equations of state [3,6,7,24,25]).

As the depletant size decreases considerably ($2L = 53 \text{ nm}$) at a slightly higher temperature ($T = 37^\circ\text{C}$) in parts E, F in Figs. 1 and 3, depletion attraction between particles with each other and all surface locations vanishes, since the excluded volume becomes identically zero in all potentials. In this case, particles explore potential energy landscapes determined by multi-particle packing effects

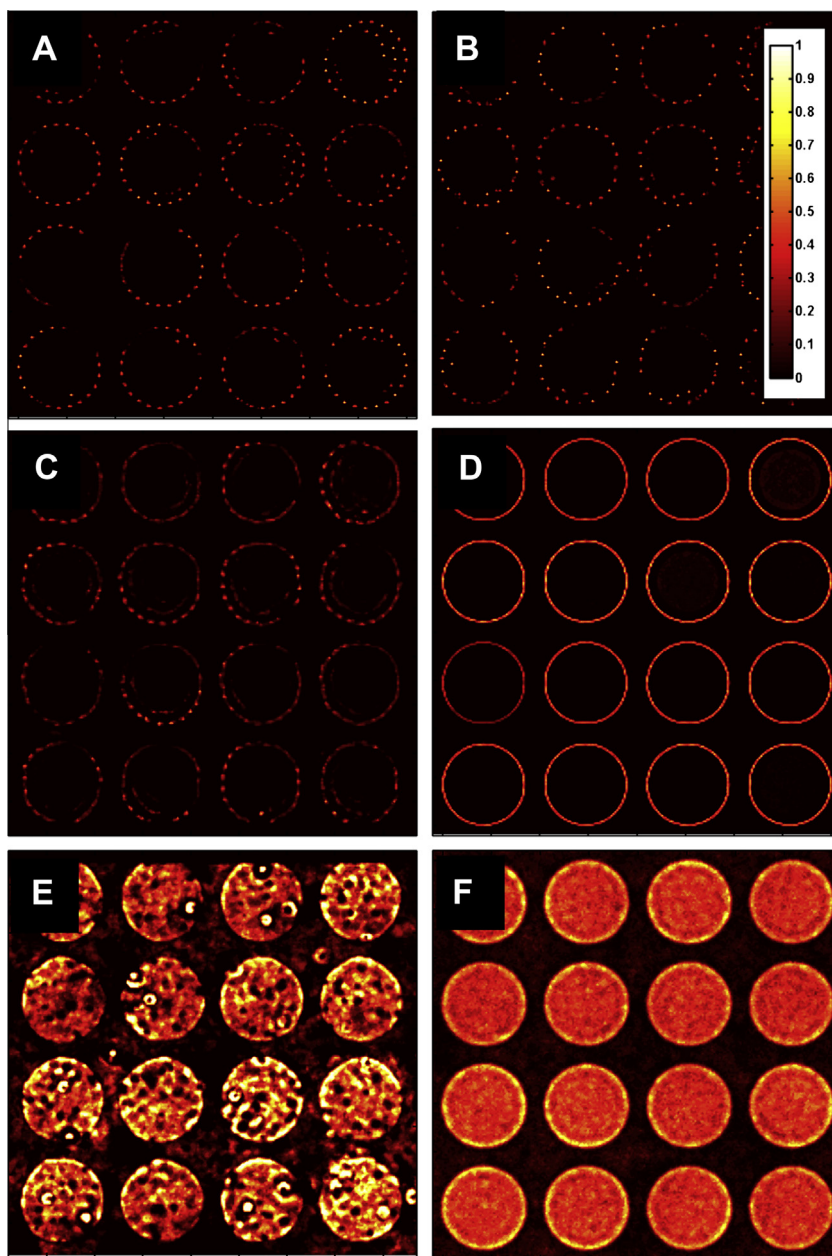


Fig. 3. 2D density landscapes from experiments (A, C, E) and simulations (B, D, F) at 25 °C, $2L = 113$ nm (A, B), 35 °C, $2L = 107$ nm (C, D), 37 °C, $2L = 53$ nm (E, F).

and gravity (i.e. elevation), similar to our previous studies [6,7,23]. The depletant size changes continuously vs. temperature, although somewhat more steeply in the vicinity of 35–37 °C, so the excluded volume, depletion potentials, and particle configuration on the underlying pattern also change more dramatically in this temperature range.

4.2. 2D free energy landscapes

In addition to comparing the experimental and simulated density profiles, Fig. 4 shows a comparison of free energy landscapes, $w(x, y)$, for the three cases in Figs. 1 and 3. The $w(x, y)$ are obtained from a Boltzmann inversion (Eq. (13)) of the density profiles in Fig. 3, which produces energy minima at the highest density positions in Fig. 3. Because $\rho(x, y)$ were matched between experiment and simulation in Fig. 3, the $w(x, y)$ also naturally agree. For the 25 °C case in Fig. 4, the particles experience $>10kT$ of depletion attraction with the pattern feature compared to all other locations

on the surface. Because $w(x, y)$ can only be constructed where particles sample, and they do not sample significantly other regions beside the pattern feature edge, it is not possible to determine the absolute depth of the energy minimum relative to the rest of the surface; it is $>10kT$, but not clear by how much. In short, particles only sample pattern feature edges in wells that are deep enough that they do not escape, so they appear to be irreversibly bound on the observation time of our experiments.

As temperature is increased to 35 °C, the attraction of particles to the pattern feature is $\sim 3kT$ lower energy than the interior of the pattern feature and $>5kT$ lower than outside the pattern feature edge. Because particle–particle interactions become weak enough that particles can sample the pattern interior, the $\sim 3kT$ difference is accurately measured. However, the depletion attraction between particles and the pattern edge plus the additional effect of gravity to escape the lower elevation interior region are too great to obtain sufficient statistics from particles outside the pattern feature. Finally, in the absence of depletion attraction at 37 °C, there is no

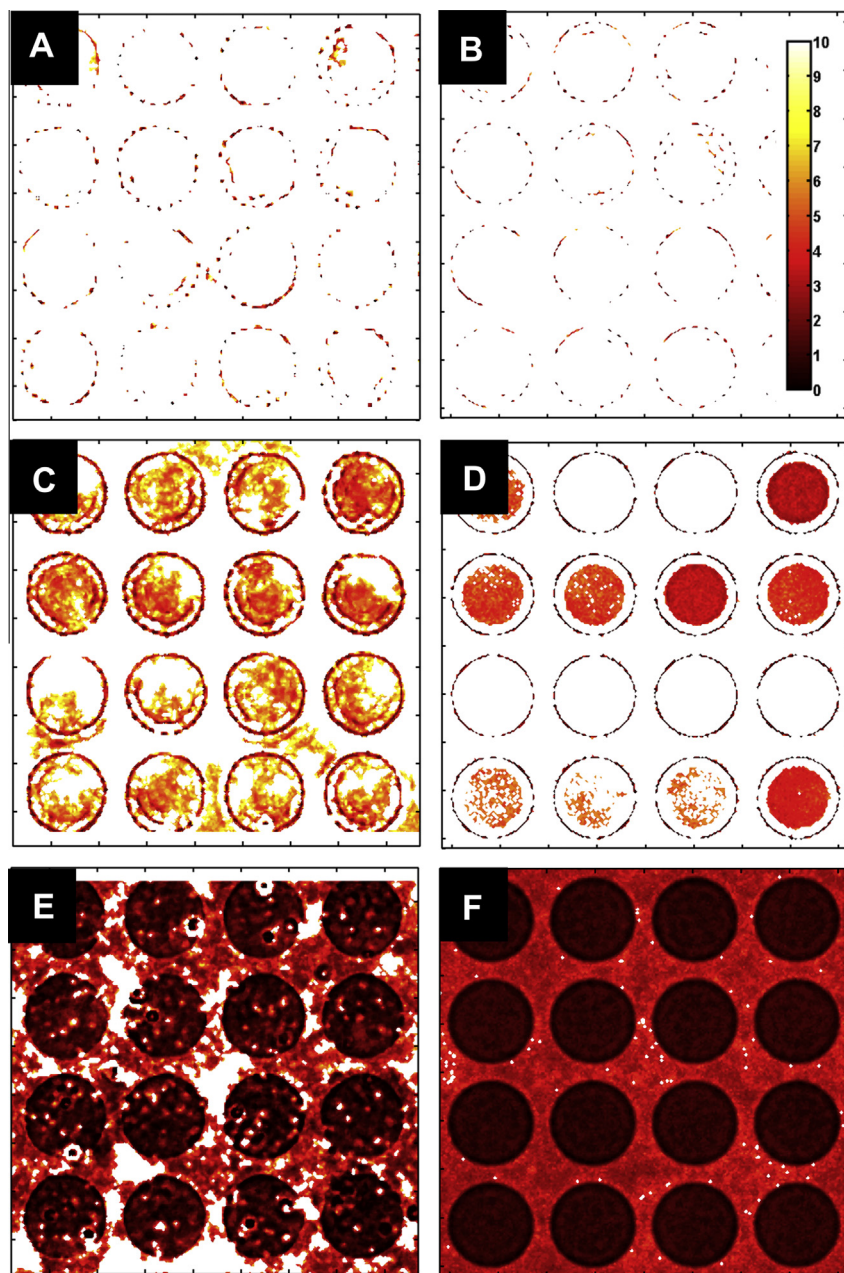


Fig. 4. 2D free energy landscapes from experiments (A, C, E) and simulations (B, D, F) at 25 °C, $2L = 113$ nm (A, B), 35 °C, $2L = 107$ nm (C, D), 37 °C, $2L = 53$ nm (E, F).

attraction to the pattern feature edge, and the free energy difference between the well interior and well exterior is $\sim 4kT$, which is close to the gravitational potential energy of particles escaping the well. The differences between free energy and potential energy landscapes at each temperature are discussed in more detail in the followings sections.

4.3. 1D density and free energy landscapes

To generate more statistics in the experimental density and energy landscapes, and to take advantage of the pattern periodicity and circular symmetry, the density profiles in Fig. 3 are: (1) averaged over all features, which are considered to be nearly identical within the spatial limits of the microfabrication methods used to generate the pattern, and (2) after converting to polar coordinates, averaged over the angular coordinate, which the density and

energy are not expected to have any dependence. This yields 1D radial density landscapes for each temperature, which are reported on the left hand side of Fig. 5. The 1D radial free energy landscapes are obtained from a Boltzmann inversion of the 1D density profiles and reported on the right hand side of Fig. 5. These results now show most clearly how the temperature dependent particle density and free energy vary relative to the pattern feature edge including the inner and outer radius of the sloped region. The oscillations in both landscapes clearly capture packing effects.

These results show at 25 °C that particles are attracted to the pattern feature edge and to each other as evident from the global energy minimum at the pattern periphery (particle-feature attraction) and the local minimum at $\sim 1.5a$ away from the edge towards the pattern interior (particle-particle attraction). The diminished single well at 35 °C quantifies the strength to which particles are attracted to the feature edge, and the absence of another well

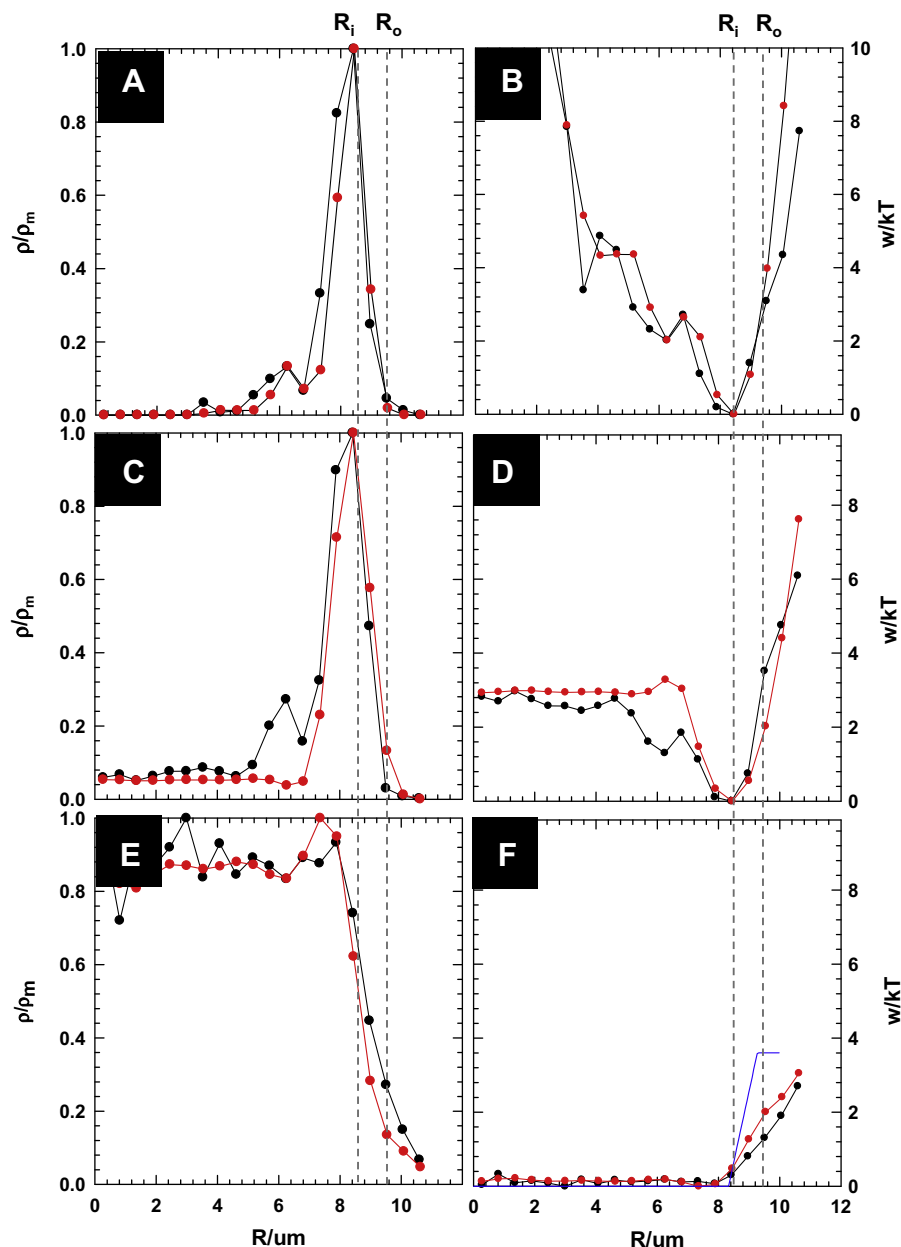


Fig. 5. 1D density (A, C, E) and free energy (B, D, F) landscapes from experiments (red lines and symbols) and simulations (black lines and symbols) at 25 °C, $2L = 113$ nm (A, B), 35 °C, $2L = 107$ nm (C, D), 37 °C, $2L = 53$ nm (E, F). Blue line in (E) is gravitational potential energy landscape. Dash lines show inner (R_i) and outer (R_o) of pattern radius. (For interpretation of the references to color in this figure legend, the reader is referred to the web version of this article.)

shows that particle–particle attraction is negligible. In the absence of depletion attraction at 37 °C, particles are no longer preferentially attracted to the pattern edge. The free energy landscape depends on the balance of gravity and multi-particle packing effects, although the extent of multi-particle packing effects has yet to be determined. As a preliminary estimate, Fig. 5F shows the potential energy landscape due to single particles on the underlying pattern, which shows how multi-particle packing effects alter the interaction compared to single particles sampling. Although multi-particle packing effects were demonstrated to “push” particles out of patterned well features in more concentrated systems [23], here the effect is less obvious. This effect is explored in more detail in the potentials obtained from the inverse MC analysis used to match the images, density landscapes, and free energy landscapes in Figs. 1–5.

4.4. Potential energy landscapes

By matching the experimental and simulated images, density, and free energy landscape in Figs. 1 and 3–5, all contributing interaction potentials are determined, which means these can be discussed in addition to the free energy landscapes reported thus far. As described in the theory section, single particles can sample a potential energy landscape, $u(x, y)$, mediated by gravitational body forces and electrostatic and depletion colloidal forces. As particles become more concentrated, multi-particle packing influences how particles sample the underlying surface via a free energy landscape (that also includes an “entropy” landscape where $w(x, y) = u(x, y) - Ts(x, y)$). MC simulations naturally account for multi-particle packing effects, so that all particle–particle and particle–substrate interaction potentials are obtained unambiguously.

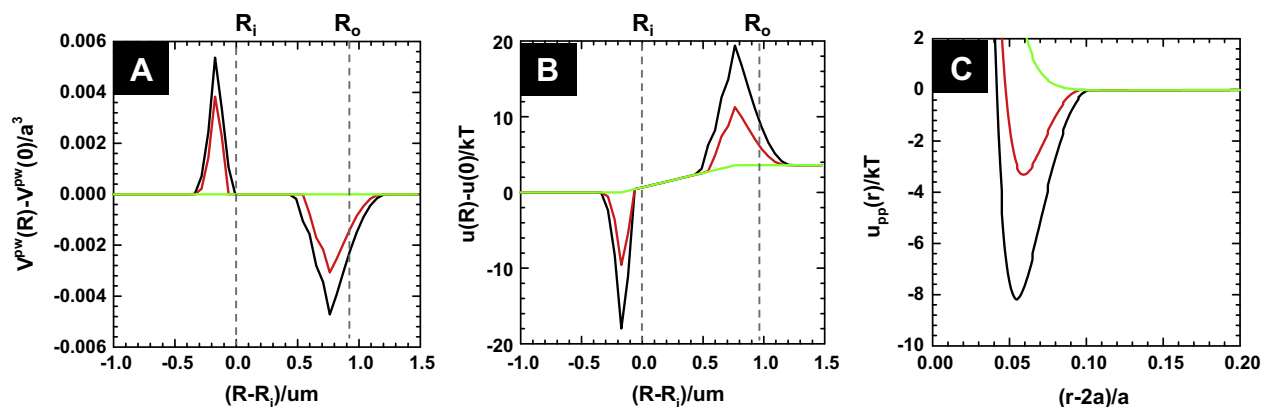


Fig. 6. Excluded volume difference (A), theoretical potential energy landscape (B), particle pair potential at 25 °C, $2L = 113$ nm (black), 35 °C, $2L = 107$ nm (red), 37 °C, $2L = 53$ nm (green). (For interpretation of the references to color in this figure legend, the reader is referred to the web version of this article.)

To understand the relevant potential energy contributions, Fig. 6 shows the radial and temperature dependence of: (A) the particle–substrate excluded volume (that determines attraction), (B) the particle–substrate potential energy landscape including electrostatics, depletion, and gravity (u^{pw} and u^{pf} in Eq. (10), electrostatic u^{pw} omitted but effectively considered from most probable elevation in Eqs. (8) and (9)), and (C) the net particle–particle separation dependent potential energy including electrostatics and depletion (u^{pp} in Eq. (1)).

The results in Fig. 6A report the excluded volume as a difference between the value computed from the numerical method and the particle–wall value given in Eq. (7). This difference is reported as a function of lateral distance to the pattern feature edge for each temperature (i.e., different depletant sizes, $2L$). When the particle is far away from the pattern edge ($R \ll R_i$, $R \gg R_o$), there is no excluded volume difference. At 37 °C, $\Delta V_{EX} = 0$ everywhere since the 53 nm PNIPAM particles are not excluded anywhere between the particles and patterned surface. At 35 °C and 25 °C, ΔV_{EX} increases with increasing $2L$ at the inner edge of the feature, where the concave surface curvature complements the particle, and decreases at the outer edge, where the convex curvature bends away from the particle surface.

Fig. 6B shows a plot of the potential energy landscape vs. the radial pattern feature coordinate. Potential energy is plotted related to the energy at the pattern feature center, where particle–wall electrostatics, depletion, and gravity balance each other to produce a most probable elevation (i.e., Eq. (8)). For $T = 37$ °C, $\Delta V_{EX} = 0$ everywhere, and a purely gravitational potential energy landscape is obtained due to the elevation change of the surface. This explains the higher density of particle inside the pattern features. By multiplying the depletant osmotic pressure by ΔV_{EX} at 25 °C and 35 °C from Fig. 6A and adding it to the gravitational potential energy landscape, it is possible to obtain the potential energy landscape due to both contributions. It is now easy to see that single particles experience $\sim 10kT$ of attraction to the concave inner feature edge at 35 °C and nearly $\sim 20kT$ of attraction at 25 °C. In addition, the reduced excluded volume at the convex outer edge produce $\sim 5kT$ and $\sim 15kT$ potential energy barriers to single particles escaping the pattern outer edge. Together, the energy minimum at the inner edge and energy maximum at the outer edge produce energy changes (minimum depth to barrier maximum) of $\sim 15kT$ and $\sim 35kT$, which is effective at preventing particle escape immobilizing particles with energies $\gg kT$.

Finally, Fig. 6C also shows the pairwise particle–particle depletion attraction that contributes to the free energy landscapes in Fig. 5. The $\sim 8kT$ and $\sim 3kT$ particle–particle attraction at 25 °C and 35 °C are consistent with the degree of particle attachment

to the first layer of particles immobilized at the pattern feature edge. In particular, the second layer of particles is completely immobile at 25 °C, whereas this layer shows intermittent attachment and detachment at 35 °C. At 37 °C, all depletion attraction vanishes including the particle–particle, particle–wall, and particle–edge feature attraction. The patterned surface mediated potential energy landscapes in combination with particle pair potentials reported in Fig. 6, when combined with multi-particle packing effects (i.e., entropic contributions), clearly capture the free energy landscapes and density profiles obtained in the experimental studies reported in Fig. 1.

5. Conclusions

Our results demonstrate the ability to accurately interpret and predict excluded volume effects between colloids with each other and topographically patterned surfaces in the presence of depletants with thermosensitive sizes. A new modeling approach is reported to numerically compute the excluded volume between colloids interacting with arbitrary surface geometries. This approach enables the computation of depletion attraction with local surface pattern features in the presence of depletants with varying dimensions. This method is used to match Monte Carlo simulations to experiments to model the temperature dependent density, free energy, and potential energy landscapes that determine non-close-packed colloidal configurations on periodic arrays of circular features. Ultimately, the ability to quantitatively understand the interplay of electrostatic, gravitational, and tunable depletion interactions on topographically patterned substrates provides a basis to design and control colloidal based reconfigurable materials and devices for micro- and nano-technologies.

Acknowledgment

We acknowledge financial support by the National Science Foundation (CBET-1234981).

References

- [1] S. Asakura, F. Oosawa, J. Chem. Phys. 22 (7) (1954) 1255–1256.
- [2] H.N.W. Lekkerkerker, R. Tuinier, Colloids and the Depletion Interaction, Springer, Berlin, 2011, p. 234.
- [3] T.D. Edwards, M.A. Bevan, Langmuir 28 (39) (2012) 13816–13823.
- [4] D. Marenduzzo, K. Finan, P.R. Cook, J. Cell Biol. 175 (5) (2006) 681–686.
- [5] J.R. Savage, D.W. Blair, A.J. Levine, R.A. Guyer, A.D. Dinsmore, Science 314 (2006) 795–798.
- [6] G.E. Fernandes, D.J. Beltran-Villegas, M.A. Bevan, Langmuir 24 (2008) 10776–10785.

- [7] G.E. Fernandes, D.J. Beltran-Villegas, M.A. Bevan, *J. Chem. Phys.* 131 (2009) 134705.
- [8] L.T. Shelley, E. Robert, C.P. Royall, *J. Phys.: Condens. Matter* 24 (46) (2012) 464128.
- [9] A. Trokhymchuk, D. Henderson, A. Nikolov, D.T. Wasan, *J. Colloid Interface Sci.* 243 (1) (2001) 116–127.
- [10] A.D. Nikolov, D.T. Wasan, *J. Colloid Interface Sci.* 133 (1) (1989) 1–12.
- [11] A.D. Dinsmore, A.G. Yodh, D.J. Pine, *Nature* 383 (6597) (1996) 239–242.
- [12] K.-H. Lin, J.C. Crocker, V. Prasad, A. Schofield, D.A. Weitz, T.C. Lubensky, A.G. Yodh, *Phys. Rev. Lett.* 85 (8) (2000) 1770–1773.
- [13] W. Lee, A. Chan, M.A. Bevan, J.A. Lewis, P.V. Braun, *Langmuir* 20 (13) (2004) 5262–5270.
- [14] Sp. Badaire, Cc. Cottin-Bizonne, A.D. Stroock, *Langmuir* 24 (20) (2008) 11451–11463.
- [15] K. Zhao, T.G. Mason, *Phys. Rev. Lett.* 101 (2008) 148301.
- [16] S. Sacanna, W.T.M. Irvine, P.M. Chaikin, D.J. Pine, *Nature* 464 (7288) (2010) 575–578.
- [17] T.D. Edwards, Y. Yang, M.A. Bevan, Reconfigurable multi-scale colloidal assembly on excluded volume patterns, 2014 (in preparation).
- [18] K.A. Arpin, A. Mihi, H.T. Johnson, A.J. Baca, J.A. Rogers, J.A. Lewis, P.V. Braun, *Adv. Mater.* 22 (10) (2010) 1084–1101.
- [19] G.M. Bell, S. Levine, L.N. McCartney, *J. Colloid Interface Sci.* 33 (3) (1970) 335–359.
- [20] W.B. Russel, D.A. Saville, W.R. Schowalter, *Colloidal Dispersions*, Cambridge University Press, New York, 1989.
- [21] A. Vrij, *Pure Appl. Chem.* 48 (1976) 471–483.
- [22] A. Sharma, J.Y. Walz, *J. Chem. Soc., Faraday Trans.* 92 (24) (1996) 4997–5004.
- [23] P. Bahukudumbi, M.A. Bevan, *J. Chem. Phys.* 126 (2007) 244702.
- [24] T.D. Iracki, D.J. Beltran-Villegas, S.L. Eichmann, M.A. Bevan, *Langmuir* 26 (2010) 18710–18717.
- [25] T.D. Edwards, M.A. Bevan, *Macromolecules* 45 (1) (2012) 585–594.
- [26] H.J. Wu, M.A. Bevan, *Langmuir* 21 (4) (2005) 1244–1254.
- [27] H.-J. Wu, T.O. Pangburn, R.E. Beckham, M.A. Bevan, *Langmuir* 21 (22) (2005) 9879–9888.